Available online at www.sciencedirect.com
ScienceDirect
Acta Materialia 57 (2009) 1755–1767
Acta MATERIALIA
www.elsevier.com/locate/actamat

Lattice Boltzmann modeling of dendritic growth in a forced melt convection

Dongke Sun [a], Mingfang Zhu [a,*], Shiyan Pan [a], Dierk Raabe [b]

[a] Jiangsu Key Laboratory for Advanced Metallic Materials, School of Materials Science and Engineering, Southeast University, Nanjing, Jiangsu 211189, China
[b] Max-Planck-Institut für Eisenforschung, 40237 Düsseldorf, Germany

Received 18 August 2008; received in revised form 12 December 2008; accepted 12 December 2008
Available online 29 January 2009

Abstract

A two-dimensional (2D) lattice Boltzmann-based model is developed to simulate solutal dendritic growth of binary alloys in the presence of forced flow. The model adopts the lattice Boltzmann method (LBM) that describes transport phenomena by the evolution of distribution functions of moving pseudoparticles to numerically solve fluid flow and solute transport governed by both convection and diffusion. Based on the LBM-calculated solutal field, the dynamics of dendritic growth is determined according to a previously proposed local solutal equilibrium approach. After detailed model analysis and validation, the model is applied to simulate single and equiaxed multidendritic growth of Al–Cu alloys with forced convection. The results demonstrate the quantitative, numerically stable and computationally efficient capabilities of the proposed model. It is found that the solute distribution and dendritic growth are strongly influenced by convection, producing asymmetrical dendrites that grow faster in the upstream direction, but mostly slower in the downstream direction.

Keywords: Modeling; Dendritic growth; Lattice Boltzmann method; Convection; Diffusion

1. Introduction

Dendritic microstructures, which are commonly observed in solidification of metallic materials, mostly determine the mechanical integrity of castings. The solidification is known to be always accompanied by melt convection which may significantly alter the pattern formation of dendritic microstructures and the solute distribution. The coupling mechanisms between the development of solidification microstructure and melt convection have been of great interest for both academic research and practical application.

In parallel to the advances of experimental techniques and analytical models, numerical models have been developed to understand the dendritic growth and microstructure formation in solidification for some years [1–12]. Numerical studies on the interaction of melt convection and dendritic growth in pure materials and alloys have been performed using phase-field (PF) methods [1–4], a front tracking method [5], level set (LS) methods [6,7] and cellular automaton (CA) methods [8–12].

PF models have been applied successfully to reproduce the typical asymmetric features of dendritic growth with undercooled melt convection [1–4]. Tong et al. [2] developed a PF model incorporating the solution of the Navier–Stokes (NS) equation and thermal noise to simulate the free thermal dendritic growth of a pure substance in forced melt convection. The simulated results based on a parabolic fitted tip radius are found to agree well with the Oseen–Ivantsov solution and the linearized solvability theory. Lan and Shih carried out adaptive PF simulations of isothermal and non-isothermal free dendritic growth for a nickel/copper binary alloy system with forced convection

---

[*] Corresponding author. Tel.: +86 25 83793355.
E-mail address: zhumf@seu.edu.cn (M. Zhu).

1359-6454/$36.00 © 2008 Acta Materialia Inc. Published by Elsevier Ltd. All rights reserved.
doi:10.1016/j.actamat.2008.12.019

[3,4]. In the isothermal environment, the simulated results with an antisolutal trapping scheme are in good agreement with the Oseen–Ivantsov solution for concentration-driven dendritic growth with convection. The selection scaling factor increases with the external flow as the prediction of the linearized solvability theory [3].

Tan et al. [6,7] proposed a LS method combining features of front tracking and fixed domain for modeling dendritic growth during the solidification of pure metal and alloys. In their model the melt flow is described using an equal-order velocity–pressure interpolation of the NS equation. The solid/liquid (SL) interface is treated as a narrow mushy zone and volume-averaging is used for energy, species and momentum transports to the mushy zone. The adaptive mesh refinement approach adopted in the model allows the simulations of coupling the microstructure evolution at the mesoscale with buoyancy-driven flow in the macroscale [6,7].

Models based on cellular automata (CA) have also been developed to simulate the evolution of dendritic morphology during alloy solidification in the presence of melt convection [8–12]. The models are capable of simulating convective single- and multidendritic growth with acceptable computational efficiency [9–11]. Li et al. validated the CA model and found that the calculated data with fine mesh agree well with the Oseen–Ivanstov solution for isothermal concentration-driven dendritic growth in a fluid flow [12].

In all the above numerical models, the fluid flow calculation is based on solving the NS equation using a finite difference method (FDM), finite volume method (FVM) or finite element method (FEM). Since the NS solvers are continuum-based approaches, it is not easy to properly handle the discontinuity of flow velocity at the moving SL interface. Moreover, the fluid flow calculation may be difficult to converge as the dendritic morphology becomes complicated with the increase in solid fraction. In our previous work using a NS solver, we found that for solid volume fractions above 0.3 the fluid flow calculations in the simulations no longer converged.

Over the last two decades, the lattice Boltzmann method (LBM) has rapidly emerged as a comparatively powerful technique with great potential for numerically solving momentum, energy and species transport problems [13–18]. Unlike conventional macroscopic continuum-based NS solvers, the LBM is a mesoscopic kinetic-based approach that assumes the fluid flow to be composed of a collection of pseudoparticles represented by a distribution function. The macroscopic flow phenomena are characterized by the motion, collision and redistribution of these quasiparticles in the system [13]. As a computational tool, the LBM treats the nonlinear convective term through relaxation to a local equilibrium. The streaming is always local and the collision is always linear. However, in the NS solvers the transport term $\mathbf{u}\,\nabla\,\mathbf{u}$ is nonlocal and nonlinear at the same time [14]. Accordingly, the LBM has the attractive advantages of simplicity of programming, high computational performance associated with good numerical stability and time-efficiency. In addition, the LBM can be easily extended to calculate the heat and solute transports including convection and diffusion. It is particularly capable of simulating complex fluid systems, such as multiphase and multicomponent flow phenomena under complicated geometrical boundary conditions [13–18].

Owing to the basic nature of the method, it seems appropriate to couple the LBM and related simulation techniques in order to model the interaction of phase transformation and flows. Miller and co-workers [19,20] combined a LBM with enhanced collisions for hydrodynamics and heat transport together with a reaction model for the anisotropic liquid–solid phase transition. The single free dendritic growth of pure metal with moderate buoyancy convection was simulated. They then constructed a PF-based model for crystal growth in the framework of the LBM. The calculated steady-state tip velocity of dendritic growth in a static undercooled melt compared well with that predicted by solvability theory. The simulation example of three dendrites growing in an undercooled flow melt reproduces the interaction between dendritic pattern formation and buoyancy convection caused by the temperature difference between upheated crystals and cold melt [21]. Medvedev and Kassner [22] further developed the PF-LBM model. The phase transition was modeled by the PF approach proposed by Karma and Rappel. On the other hand, the flow of the liquid and heat transport were computed using the LBM. Based on this combined model, the dendritic and doublonic growth from an undercooled melt with an external flow was simulated. The relationships between the selection parameter and the Péclet number at various undercoolings and Prandtl numbers were found to be nearly on a single curve for both dendrites and doublons, respectively. It was also observed that external flow might promote the morphology transition from doublons to dendrites and change the kinetic phase diagram [23]. Chatterjee and Charkraborty developed a hybrid enthalpy-based lattice Boltzmann method (E-LBM) by coupling a modified thermal lattice Boltzmann model with an adapted enthalpy–porosity technique to simulate convection–diffusion transport involved in the liquid/solid phase transition problems. To validate the model, they compared the simulated single-convective dendritic morphology with that from the PF-NS model proposed by Beckermann et al. [1]. The authors claimed that the E-LBM model is computationally more convenient to implement for solving complex phase change problems during solidification [24].

The numerical studies on the dendritic growth in flows using the PF-LBM and E-LBM techniques have revealed that LBM is indeed very promising as an efficient computational tool for the modeling of transport phenomena coupled with phase transformation during solidification. It is noted that all the above-mentioned studies of LBM have mostly focused on free dendritic growth with convection in pure substance. However, little work has been reported about the application of LBM to the stimulation of the convective dendritic growth in alloy solidification.

This paper presents a two-dimensional (2D) LBM-based model for the simulation of solutal dendritic growth during alloy solidification in the presence of forced flow. In the model, the LBM is adopted for the simultaneous numerical calculations of melt convection and solute transport. The kinetics of the SL interface evolution is determined using a local interface composition equilibrium approach previously proposed by Zhu and Stefanescu (ZS) [25], which allows the accurate simulation of dendrite growth from the initial unstable stage to the steady-state stage without the need for a kinetic parameter. Extensive model validations, including solute diffusion, fluid flow through obstacles, purely diffusive dendritic growth and convective dendritic growth, are performed by comparing the simulations to analytical models. The proposed model is then applied to simulate both single and equiaxed multidendritic growth of Al–Cu alloys in a forced fluid flow.

2. Model description, governing equations and numerical algorithms

2.1. Model description

In the present study, solutal dendritic growth of binary alloys in the presence of melt convection is considered to take place in the low Péclet number and low Reynolds number regime. The driving force for dendritic growth is determined using a local composition equilibrium approach [25]. According to this approach, the kinetics of dendritic growth is related to the difference between the local equilibrium composition and the local actual liquid composition. The local equilibrium composition is calculated from the local temperature and curvature, whereas the local actual liquid composition is obtained by the solutal transport calculation. Fig. 1 illustrates the physical system under consideration. The 2D computational domain is divided into a uniform orthogonal arrangement of cells. Each cell is characterized by several variables of flow vector, concentration, crystallographic orientation, solid fraction, etc., and marked as the state of liquid, solid or interface. Since the emphasis of the present work is on solute-driven dendritic growth in a fluid flow, for the sake of simplicity, the temperature field inside the domain is considered to be uniform with a constant undercooling or cooling down with a constant cooling rate. The buoyancy-driven flow due to gravity is neglected. The forced flow is generated by imposing a uniform inlet flow velocity indicated as U_{in} at the left boundary of the domain. The undercooled melt, taken as an incompressible Newtonian fluid, comes into the domain from the left boundary, flows past the solidified cells, and then goes out from the right wall of the domain. At the beginning of the simulation, one or several solid seeds are placed on the domain. When a crystal is suspended in an undercooled melt of a hypoeutectic alloy, the local interface equilibrium composition is larger than the local actual liquid composition. In order to reach the equilibrium composition, solidification begins. As the dendrite grows, solute is released at the SL interface, which results in a solutal gradient ahead of the interface, leading to solute transport in the domain. In the presence of melt convection, the solute transport is controlled by both diffusion and convection. Since convection vanishes in the solid and the solute diffusion coefficient in the solid phase is about three orders of magnitude smaller than that in the liquid, for the sake of simplicity, solid diffusion is ignored and the solute transport is only computed in the liquid phase. The solute transfer, governed by convection and diffusion, will result in a new solute field which determines the local actual interface liquid composition. The growing dendrite, assumed to be rigid and stationary, in turn triggers an increasing complex fluid flow and also changes the interface curvature which influences the interface equilibrium composition. This interaction of fluid flow, solute transport and dendritic growth continues to the end of solidification. The governing equations and numerical algorithms for calculating fluid flow, solute field, interface curvature, crystallographic anisotropy and kinetics of dendritic growth are described in detail below.

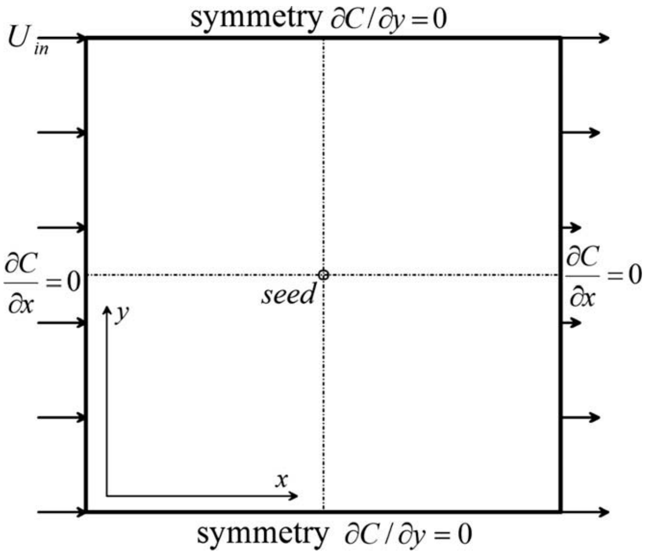

Fig. 1. Illustration of the physical system and boundary conditions used in the simulations.

2.2. Lattice Boltzmann method for the calculation of fluid flow and solute transport

In the present work, the LBM is adopted to numerically calculate the fluid flow and solute transport. The LBM originates from the gas kinetic theory based on the classical Boltzmann equation. A widely used approximation of the Boltzmann equation is the Bhatnagar–Gross–Krook (BGK) approach in which the collision term is approximated by a single relaxation time scheme [26,27]. The evolution equation of the lattice BGK (LBGK) model is expressed as:

$$f_i(\mathbf{x}+\mathbf{e}_i\Delta t, t+\Delta t) - f_i(\mathbf{x},t) = -[f_i(\mathbf{x},t) - f_i^{eq}(\mathbf{x},t)]/\tau + F_i(\mathbf{x},t), \quad (1)$$

where $f_i(\mathbf{x},t)$ is the particle distribution function (PDF) representing the probability of finding a pseudoparticle at location $\mathbf{x}$ and time t, $\mathbf{e}_i$ is the discrete moving velocity of the pseudoparticle, Δt is the time step, τ is the relaxation time, $f_i^{eq}(\mathbf{x},t)$ is the equilibrium distribution function, and $F_i(\mathbf{x},t)$ is the force term caused by the internal interaction or external fields such as gravity and magnetic force. As described previously, in the present work, the buoyancy effect caused by gravity is ignored and the forced flow is introduced by a uniform inlet flow velocity. Thus, the force term in Eq. (1), $F_i(\mathbf{x},t)$, is taken to be zero.

The LBM also can be used to calculate solute transport controlled by both convection and diffusion. Similar to the LB equation for fluid flow calculation, the solute distribution function $g_i(\mathrm{x},t)$ with the source term can be written as [28]:

$$g_i(\mathbf{x}+\mathbf{e}_i\Delta t, t+\Delta t) - g_i(\mathbf{x},t) = -[g_i(\mathbf{x},t) - g_i^{eq}(\mathbf{x},t)]/\tau_D + S_i(\mathbf{x},t), \quad (2)$$

where τ_D and $g_i^{eq}(\mathbf{x},t)$ are the relaxation time and the equilibrium distribution function for the solute transport calculation, respectively. The source term in Eq. (2), $S_i(\mathbf{x},t)$, denotes the amount of solute rejected at the SL interface during dendritic growth.

A widely used 2D nine-velocity (D2Q9) LB model [27] is employed in the present work. In the D2Q9 model, space is discretized into a square lattice including nine discrete velocities, $\mathbf{e}_i$, which are given by

$$\mathbf{e}_i = \begin{cases} (0,0) & i=0, \\ (\cos[(i-1)\pi/2], \sin[(i-1)\pi/2])c & i=1\text{–}4, \\ (\cos[(2i-9)\pi/4], \sin[(2i-9)\pi/4])\sqrt{2}c & i=5\text{–}8, \end{cases} \quad (3)$$

where $c = \Delta x/\Delta t$ is the lattice speed, Δx is the lattice spacing, Δt is the time step. The macroscopic variables such as fluid density, ρ, velocity, $\mathbf{u}$ and composition, C, can be calculated from the relevant distribution functions, respectively:

$$\rho = \sum_{i=0}^{8} f_i, \quad \rho\mathbf{u} = \sum_{i=0}^{8} f_i\mathbf{e}_i, \quad C = \sum_{i=0}^{8} g_i. \quad (4)$$

In the D2Q9 scheme, the equilibrium distribution functions in Eqs. (1) and (2) are defined as

$$f_i^{eq}(\mathbf{x},t) = w_i\rho\left[1 + 3\frac{(\mathbf{e}_i\cdot\mathbf{u})}{c^2} + 4.5\frac{(\mathbf{e}_i\cdot\mathbf{u})^2}{c^4} - 1.5\frac{\mathbf{u}^2}{c^2}\right], \quad (5)$$

$$g_i^{eq}(\mathbf{x},t) = w_iC\left[1 + 3\frac{(\mathbf{e}_i\cdot\mathbf{u})}{c^2} + 4.5\frac{(\mathbf{e}_i\cdot\mathbf{u})^2}{c^4} - 1.5\frac{\mathbf{u}^2}{c^2}\right], \quad (6)$$

where w_i are the weight coefficients given by $w_0 = 4/9$, $w_{1\text{–}4} = 1/9$ and $w_{5\text{–}8} = 1/36$. In Eq. (6), the terms that include the flow velocity vector, $\mathbf{u}$, represent the convection contribution to the solute transport. Apparently, in the case of $\mathbf{u} = 0$, pure solute diffusion can be calculated. According to the Chapman–Enskog analysis [29], the continuum equation, the NS equation and the convection–diffusion equation can be recovered from the above-described LB equations. The kinematic viscosity, v, and the solute diffusion coefficient, D, are related to the relaxation times τ and τ_D, respectively:

$$v = c^2\Delta t(2\tau - 1)/6, \quad D = c^2\Delta t(2\tau_D - 1)/6. \quad (7)$$

Boundary conditions are very important for the accuracy and stability of LBM simulation. The unknown particle distribution functions at the boundary nodes must be calculated through proper boundary conditions. In the present work, for flow field calculation, the nonequilibrium extrapolation scheme with second-order accuracy [30] is employed at the left and right walls of the domain, whereas the top and bottom walls are treated as symmetrical using periodic boundary conditions. The nonslip boundary condition is implemented at the SL interface using the bounce-back rule [31]. For solutal transport simulation, the zero-flux boundary condition is imposed on the four surfaces of the calculation domain. As mentioned previously, it is assumed that there is no solute transport in the solid phase. Thus, the bounce-back scheme is also applied at the SL interface for solutal field calculation.

2.3. Solution of the phase fraction evolution

As described in Section 2.1, in the present model the driving force for dendritic growth is considered to be controlled by the difference between local interface equilibrium composition and local actual liquid composition. Based on the thermodynamic concept of local equilibrium between liquid and solid phases, the interface equilibrium composition C_l^* can be calculated by:

$$C_l^* = C_0 + [(T^* - T_l^{eq}) + \Gamma K(1 - 15\varepsilon\cos[4(\theta-\theta_0)])]/m, \quad (8)$$

where T^* is the interface temperature, T_l^{eq} is the equilibrium liquidus temperature at the initial composition C_0, ε is the degree of anisotropy of the surface energy, m is the liquidus slope, Γ is the Gibbs–Thomson coefficient, K is the curvature of the SL interface, θ is the growth angle between the normal to the interface and the x-axis and θ_0 is the angle of the preferential growth direction with respect to the x-axis. The calculated local interface equilibrium composition is compared with the local actual liquid composition C_l which is determined by solving Eqs. (1)–(7) using the LBM. If the difference $\Delta C = C_l^* - C_l > 0$, the solid fraction of this interface cell will increase. According to the solute equilibrium condition at the interface, during one time step interval, Δt, the increased solid fraction, $\Delta\varphi_s$, of an interface cell in one time step can be evaluated by:

$$\Delta\varphi_s = (C_l^* - C_l)/[C_l^*(1-k)], \quad (9)$$

where k is the solute partition coefficient. As the solid fraction increases, solute is rejected at the SL interface. Solute partition between liquid and solid at the SL interface is considered according to $C_s = kC_l$. The rejected solute in an interface cell at each time step can be evaluated as $\Delta C = C_l(1 - k)\Delta\varphi_s$. Thus, the source term $S_i(\mathbf{x}, t)$, in Eq. (2) can be calculated with $S_i(\mathbf{x}, t) = w_i\Delta\varphi_s C_l(1 - k)$. If at time $t = t_n$, the sum of the solid fraction in an interface cell equals 1, the state of this cell is assigned as solid and new interface cells are explicitly captured. However, the exact SL front is implicitly scaled by the solid fraction within each interface cell. The local interface curvature, K, and the growth angle, θ, in Eq. (8) can be calculated according to the solid fraction gradient at the SL interface using the following equations [32]:

$$K = [2\partial_x\varphi_s\partial_y\varphi_s\partial^2_{xy}\varphi_s - (\partial_x\varphi_s)^2\partial^2_y\varphi_s - (\partial_y\varphi_s)^2\partial^2_x\varphi_s] \times [(\partial_x\varphi_s)^2 + (\partial_y\varphi_s)^2]^{-3/2} \quad (10)$$

$$\theta = \arccos(\partial_x\varphi_s/[(\partial_x\varphi_s)^2 + (\partial_y\varphi_s)^2]^{1/2}). \quad (11)$$

Eqs. (10) and (11) are solved using a centered finite-difference scheme with second-order accuracy for the partial derivatives of the solid fraction.

2.4. Numerical solution sequence

The solution sequence of the equations and algorithms described above consists of the following steps:

1. Initialing the simulation system with domain length, mesh size, flow field and composition field, solid seeds with preferential crystallographic orientations.
2. Calculating the flow field and the solutal field by solving Eqs. (1)–(6) for each cell in the whole domain. The flow velocity and liquid composition are calculated according to Eq. (4). Meanwhile, the solid composition is calculated with $C_s = kC_l$.
3. Calculating the interface curvature with Eq. (10), the interface equilibrium composition with Eq. (8), and the increase in solid fraction with Eq. (9) for each interface cell.
4. Calculating and adding the rejected solute amount $w_i\Delta\varphi_s C_l(1 - k)$ to the solute distribution function of the same interface cell. If the cell is fully solidified, it is added to the solute distribution function of its surrounding neighbor interface or liquid cells. Thus, the overall solute conservation in the domain can be maintained.
5. Next time step from Step (2) until the end of the simulation.

The physical parameters used in the present work are given in Table 1. The flow relaxation time is chosen to be $\tau = 1$ and τ_D can be computed by Eq. (7) according to the kinematic viscosity, v, and the solute diffusion coefficient in liquid, D_l. The dimensionless composition, undercooling, length, time, growth velocity and flow velocity are used by rescaling the relative quantities with C_0, $\Delta T_0 = |m|(1 - k)C_0$, $d_0 = \Gamma/\Delta T_0$, $t_0 = d_0^2/D_l$, $V_0 = D_l/d_0$ and $U_0 = v/d_0$, respectively, where ΔT_0 is the unit undercooling and d_0 is the solutal capillary length.

Table 1
The parameters used in the present work.

Symbol	Definition and units	Value
ρ	Density (kg m^{-3})	2.475×10^3
μ	Viscosity (P)	0.014
D_l	Solute diffusion coefficient in liquid (m^2 s^{-1})	3.0×10^{-9}
m	Liquidus slope (K wt.%$^{-1}$)	−2.6
k	Partition coefficient	0.17
Γ	Gibbs–Thomson coefficient (mK)	2.4×10^{-7}
ε	Degree of anisotropy of the surface energy	0.0267
d_0	Solutal capillary length (m)	3.707×10^{-8}

3. Results and discussion

3.1. Mesh dependency

To evaluate the mesh dependency of the present model, simulations are performed for a single dendrite of an Al–3 wt.% Cu alloy growing at a constant dimensionless melt undercooling $\Delta T/(|m|(1 - k)C_0) = 0.6$ with an inlet flow velocity of $U_{in}d_0/v = 0.0005$. At the beginning of the simulation, a solid seed with a preferential crystallographic orientation of 0° with respect to the horizontal direction is placed at the center of the domain. For these simulations the domain length is kept constant with $2400d_0 \times 2400d_0$, whereas the mesh size and numbers are varied. The method of determining the steady-state growth velocities of the dendrite tip is described in the next section. Fig. 2 shows the steady-state growth velocity of the upstream tip as a function of mesh size. It can be noted from Fig. 2 that the converged solution of tip velocity is obtained when the mesh size $\Delta x/d_0$ is smaller than 14. It is found that tip splitting occurs when the mesh size is larger than 14,

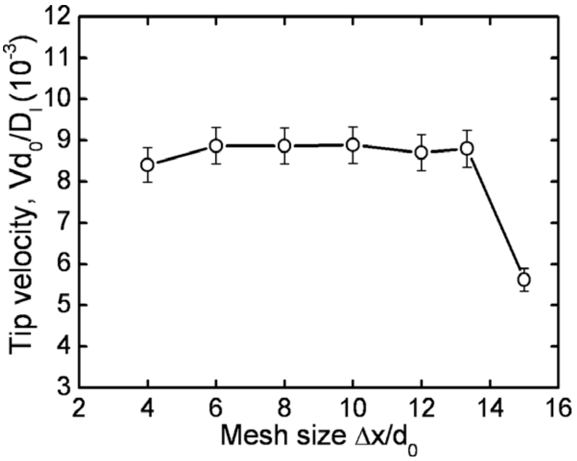

Fig. 2. Steady-state growth velocity of the upstream tip as a function of mesh size ($U_{in}d_0/v = 0.0005$, $\Delta T/(|m|(1 - k)C_0) = 0.6$).

which is considered to be the main reason for the remarkable decrease in velocity when the mesh size is out of the region of convergence.

3.2. Validation of LBM for the calculation of solute diffusion and fluid flow

To validate the LBM for the calculation of solute diffusion, a classical benchmark problem has been modeled, namely 1D solute transport with a prescribed constant composition boundary. The domain is divided into 200 lattice units in the horizontal direction with the initial composition of $C(x,0) = C_0$. The left boundary is imposed with a prescribed constant composition of $C(0,t) = C_{\mathrm{H}}$. However, the zero flux boundary condition is applied for the right boundary. In this calculation, C_H and C_0 are taken as 5.5% and 4.0%, respectively. For the 1D solute transport, the analytical solution can be obtain by

$$C = C_0 + (C_H - C_0) \cdot \left(1 - erf\left(\frac{x}{2\sqrt{Dt}}\right)\right), \tag{12}$$

where x is the distance from the left boundary, D is the diffusion coefficient and t is the time. Fig. 3 presents a comparison of the solute profiles calculated by the LBM and the analytical solution. It can be seen that the agreement between the LBM calculation and the analytical result is excellent.

The second validation is performed to confirm that the LBM is working properly in the simulation of fluid flow through obstacles with a curved interface. The model is extended to a special case described by Stokes flow through regular arrays of infinite cylinders. As illustrated in Fig. 4, a round obstacle is fixed in the computational domain. The obstacle/fluid interface is treated as nonslip boundary condition using the bounce-back rule. Periodic boundary conditions are employed on the top and bottom sides of the domain. The left and right walls are given with the velocity boundary condition of $\partial_x u_x = 0$ and $u_y = 0$ using the non-equilibrium extrapolation scheme [30]. A constant pressure gradient is imposed to generate fluid flow in the horizontal direction. Fig. 5 presents a comparison of the result obtained by the LBM for the dimensionless mean flow velocity as a function of volume fraction of obstacle with the analytical solution derived by Sangani and Acrivos [33]. As shown, the LBM calculated data approach zero as the volume fraction of obstacle increases to higher values and coincide well with the analytical profile.

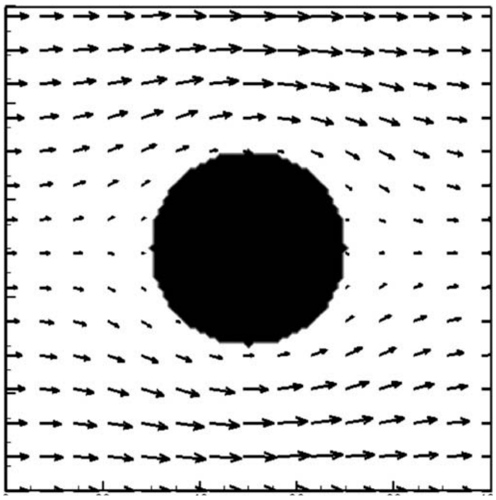

Fig. 4. The fluid flow through one round obstacle fixed in the center of the domain.

3.3. Dendritic growth in a static melt

To validate the present model for purely diffusive dendritic growth, the simulated steady-state growth features of an Al–3 wt.% Cu alloy as a function of melt undercooling are compared with the Lipton–Glicksman–Kurz (LGK) model predictions. The LGK [34,35] analytical model can be used for predicting the steady-state tip velocity and radius of a branchless needle dendrite freely growing in an undercooled static alloy melt controlled by

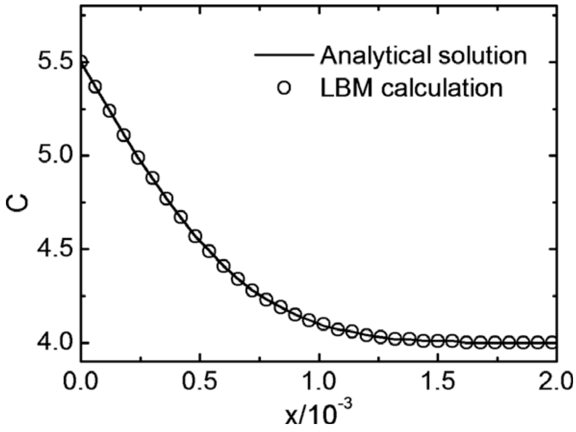

Fig. 3. Comparison between the LBM calculation and the analytical solution for the 1D solute diffusion calculation.

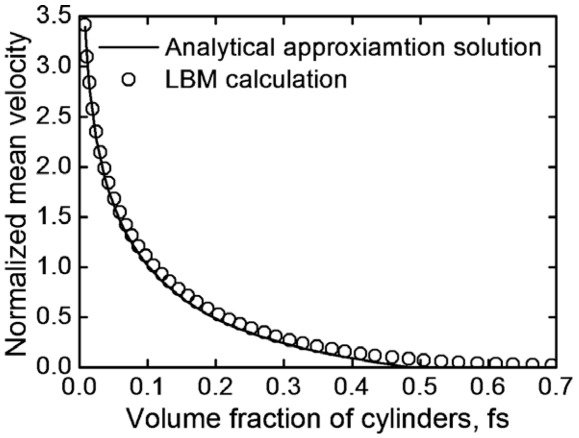

Fig. 5. Comparison of the result obtained by the LBM for the dimensionless mean flow velocity as a function of volume fraction of obstacle with the analytical solution [33].

diffusion. Since the present work deals with purely solute-driven dendritic growth during isothermal solidification of a binary alloy, thermal transport is not considered and thermal undercooling is zero. The total undercooling for purely solute-driven dendritic growth in two dimensions, ΔT, consists of solutal and curvature contributions and is given by:

$$\Delta T = \frac{|m|C_0(1-k)Iv(P_c)}{1-(1-k)Iv(P_c)} + \frac{\Gamma}{R}, \tag{13}$$

where R is the steady-state tip radius, $P_c = V \cdot R/2D_l$ is the solutal Péclet number. The 2D Ivantsov function for diffusion field can be solved by [36]:

$$Iv(P_c) = \sqrt{\pi}\sqrt{P_c}\exp(P_c) \cdot erfc(\sqrt{P_c}). \tag{14}$$

The stability criterion of the purely solutal dendritic tip is expressed as:

$$\frac{1}{\sigma^*} = \frac{V \cdot R^2}{D_l d_0[1-(1-k)Iv(P_C)]}, \tag{15}$$

where V is the steady-state tip velocity, $d_0 = \Gamma/[|m|C_0(1-k)]$ is the solutal capillary length, and σ^* is the selection parameter that is a constant equal to $1/4\pi^2$ in the marginal stability theory, whereas it is considered to be a function of the anisotropy parameter ε in the solvability theory [36,37]. We determined the selection parameter σ^* according to the linearized solvability theory derived by Barbieri and Langer [38]. When $15\varepsilon = 0.4$ was used in the present work, the corresponding σ^* for two dimensions calculated by the linearized solvability theory is 0.10654 [38]. Using this selection parameter value, The LGK-predicted steady-state tip velocity and radius as a function of melt undercooling can be obtained by solving Eqs. (13)–(15).

To minimize the influence of the domain boundary on the concentration field and to obtain a constant undercooling of the melt far away from the growing dendrite, which is the assumption of the LGK model, the simulation domain is chosen to avoid the solute diffusion layer reaching the boundary of the calculation domain. Since a dendrite growing at small undercooling needs a longer time to reach steady-state and has a wider solute diffusion layer, a larger simulation domain is required. For most cases of various undercoolings, the mesh size is chosen as $8d_0$. However, for the case of large undercooling $\Delta T/\Delta T_0 = 0.9$, a smaller mesh size of $6d_0$ is used to avoid tip splitting. At the beginning of the simulation, a solid seed with the composition of kC_0 and a preferential crystallographic orientation of $\theta°$ with respect to the horizontal direction is placed at the center of the domain. The cells surrounding the seed are assigned as interface cells. The other cells in the domain are filled with the undercooled melt liquid with the initial composition of 3 wt.% Cu. Fig. 6 shows the simulated dendrite morphology of an Al–3 wt.% Cu alloy solidified from a static undercooled melt with a dimensionless undercooling $\Delta T/(|m|(1-k)C_0) = 0.7$. The dendrite grows symmetrically in a static melt with an identical speed of four tips.

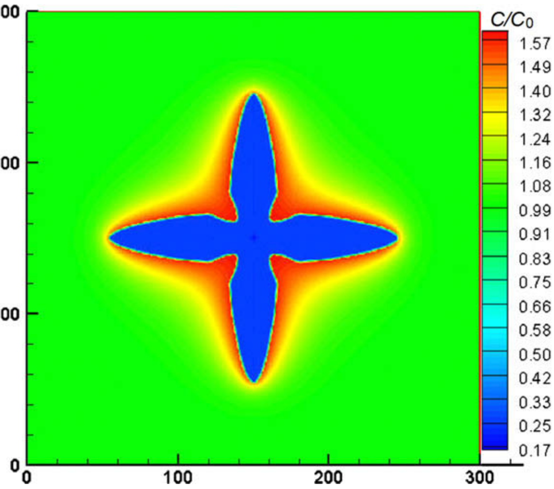

Fig. 6. Simulated dendritic morphology of an Al–3 wt.% Cu alloy solidified in a static melt at a constant melt undercooling $\Delta T/(|m|(1-k)C_0) = 0.7$.

The evolution of tip growth velocity with time is presented in Fig. 7. The growth velocities are measured from the interface cells around the dendrite tip, where the fraction of solid phase is below 0.9. Each point in the plot is an average value calculated from the measured values of several time step intervals. It is shown that the tip velocity starts from a large value and then decreases rapidly. After a transient period, the tip velocity reaches an approximately steady-state level. The transient period is of the order of D_l/V^2, where V is the steady-state tip velocity [32]. The steady-state tip velocity, tip radius and equilibrium composition are measured after at least twice this transient regime. The tip velocity and equilibrium composition are directly measured from the interface cells around the tip, and the average values are calculated. However, the tip radius is measured based on a parabolic fitting to the simulated dendrite shape as described in Ref. [25].

The comparison between the numerical simulations and the LGK predictions for the steady-state tip parameters as

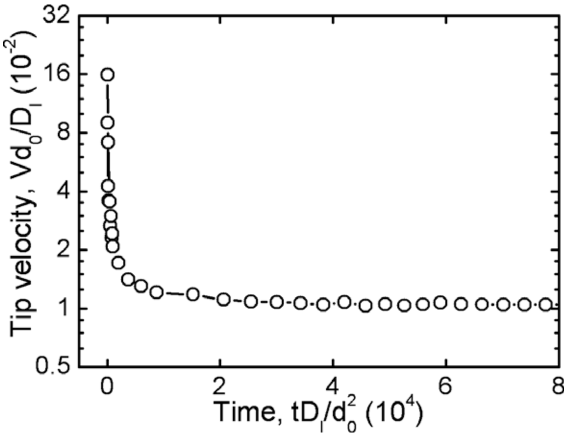

Fig. 7. Evolution of the tip growth velocity with time for the case shown in Fig. 6.

functions of the melt undercooling is presented in Fig. 8. As shown, the steady-state tip velocity, the equilibrium composition and the Péclet number increase, whereas the tip radius decreases with increasing undercooling. The steady-state tip velocity predicted by the present model is a little higher, but both, the simulated tip radius and concentration are slightly lower than the LGK results. Nevertheless, they are all close to the theoretical predictions. While some discrepancies for the Péclet number comparison can be observed at relatively higher undercoolings, the agreement between the simulation and the LGK prediction for the Péclet number is very good at relatively low undercoolings.

3.4. Dendritic growth with melt convection

3.4.1. Asymmetrical dendritic growth controlled by convection

To simulate the free dendritic growth in a forced flow, an inlet flow with a constant velocity is imposed on the left boundary of the domain. Other conditions are identical to those of Fig. 6. Fig. 9 represents the simulated dendritic morphology of an Al–3 wt.% Cu alloy growing in a flowing melt with a constant dimensionless undercooling $\Delta T/(|m|(1-k)C_0) = 0.7$ and an inlet flow velocity $U_{in}d_0/\nu = 0.0015$. Comparing Fig. 9with Fig. 6, it is apparent that the dendritic shape is significantly influenced by fluid flow. The growth of the dendrite is enhanced on the upstream side and decreased on the downstream side. Fig. 10 shows the tip velocities varying with time for the case presented in Fig. 9. While the perpendicular tip approaches an approximately steady-state velocity nearly identical to the case of pure diffusion, the state-steady velocities of the upstream and downstream tips are higher and lower, respectively, than that without flow. When the dendrite grows in the presence of convection, the solute rejected at the SL interface is washed away from the upstream to the downstream direction by the flowing melt, resulting in an asymmetrical solute profile in liquid, i.e. the concentration in the upstream region is lower than that in the downstream. Fig. 11 shows the time history of the tip concentration corresponding to the case of Figs. 9 and 10. It can be seen that the tip concentration initially rapidly increases because the rejected solute accumulates at the SL interface. After a transient period, the concentrations of different tips reach approximately stable values with different levels, indicating that the solute rejection has been balanced by the solute diffusion and convection. Moreover, the steady-state con-

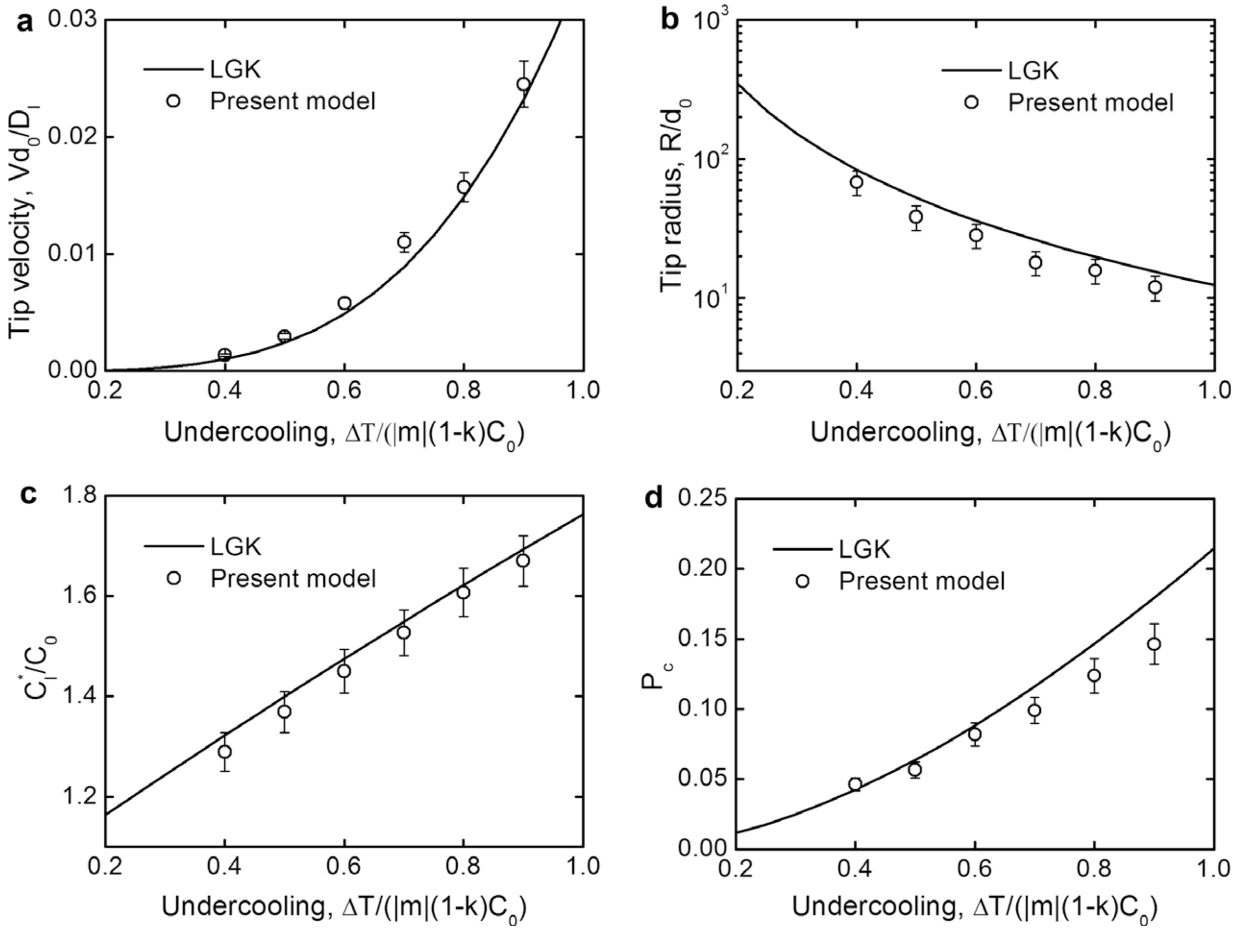

Fig. 8. Comparison between the numerical simulations and the LGK predictions for the steady-state tip parameters as functions of the melt undercooling: (a) steady-state tip velocity; (b) steady-state tip radius; (c) steady-state tip equilibrium liquid composition; (d) Péclet number.

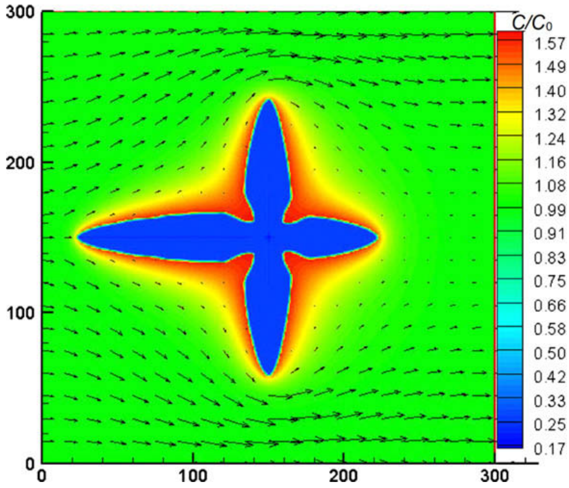

Fig. 9. Simulated dendritic morphology of an Al–3 wt.% Cu alloy growing in a flowing melt with a constant dimensionless undercooling $\Delta T/(|m|(1-k)C_0) = 0.7$ and an inlet flow velocity $U_{in}d_0/v = 0.0015$.

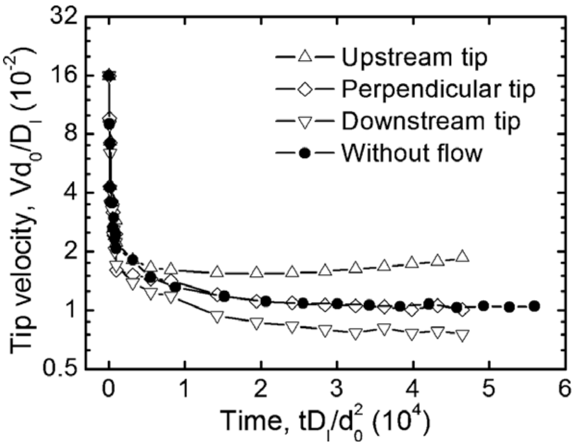

Fig. 10. Tip velocities vary with time for the case shown in Fig. 9.

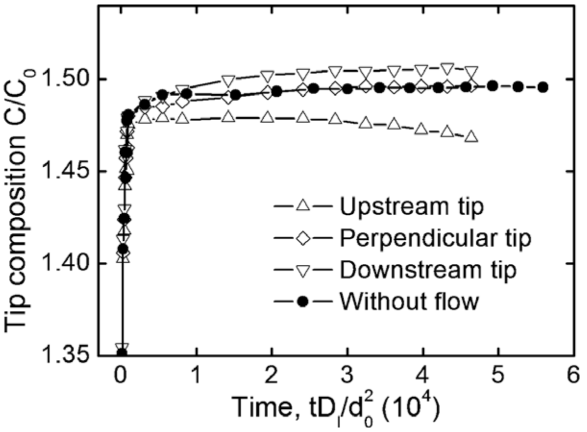

Fig. 11. Tip concentrations vary with time for the case shown in Fig. 9.

centration of the downstream tip is higher than that of the upstream tip due to the effect of convection. Under an uniform temperature field, the interface equilibrium concentration calculated by Eq. (8) will not be influenced much by fluid flow. According to Eq. (9), the decreased local actual concentration at the interface results in a higher increment in solid fraction $\Delta\varphi_s$ and thereby a higher tip velocity.

3.4.2. Comparison with the linear solvability theory

The validation of the present model for simulating dendritic growth with melt convection is attempted via comparison of the simulations against theoretical predictions. By extending the Ivantsov solution to the convection-free dendritic growth of pure substance, Bouissou and Pelce [39] derived the Oseen–Ivantsov solution that describes the steady-state dendritic growth with a forced flow in the small Reynolds number regime. Equivalent to the dendritic growth in pure materials, where the driving force is the dimensionless thermal undercooling, $\Delta = (T^* - T_\infty)/(\Delta H/C_p)$, the driving force for purely solutal dendritic growth is considered to be the dimensionless supersaturation, Ω, defined as:

$$\Omega = \frac{C_l^* - C_\infty}{C_l^*(1-k)}, \tag{16}$$

where C_∞ is the liquid composition far away from the tip. Thus, the Oseen–Ivantsov solution can also be applied to the solute-driven dendritic growth of alloys during isothermal solidification with forced convection and is given by:

$$\begin{aligned}\Omega =& P_c \exp(P_c - P_f) \\ &\times \int_1^\infty \exp\left\{-P_c\eta + P_f\left(2 + \int_1^\eta \frac{g(\zeta)}{\sqrt{\zeta}}d\varsigma - \eta\right)\right\}\frac{d\eta}{\sqrt{\eta}},\end{aligned} \tag{17}$$

where $P_c \equiv VR/(2\mathrm{D})$ is the growth Péclet number, and $P_f \equiv UR/(2\mathrm{D})$ is the flow Péclet number. The function $g(\zeta)$ in Eq. (17) is defined as:

$$g(\zeta) = \frac{\sqrt{\zeta}erfc(\sqrt{\mathrm{Re}\zeta/2}) + \sqrt{2/(\pi\mathrm{Re})}[\exp(-\mathrm{Re}/2) - \exp(-\mathrm{Re}\zeta/2)]}{erfc(\sqrt{\mathrm{Re}/2})}, \tag{18}$$

where $\mathrm{Re} \equiv UR/v$ is the Reynolds number.

It should be noted that the Oseen–Ivantsov solution is derived based on convective dendritic growth in a pure substance, where only thermal transport is calculated, and that the thermal diffusion is a two-sided problem, i.e. $\alpha_s \approx \alpha_l$, here α_s and α_l are the thermal diffusivities in solid and liquid, respectively. However, in the simulation of isothermal solute-driven dendritic growth, only solutal transport is considered, which is a one-sided problem, i.e. $D_s << D_l$. For comparison with the Oseen–Ivantsov solution, we assumed equal solid/liquid solutal diffusivities, i.e. $D_s = D_l$, for this particular simulation. To implement the $D_s = D_l$ condition, the bounce-back scheme applied at the SL interface for the LBM solutal diffusion calculation had to be dropped. The calculation domain consists of 400 × 400 mesh points with a mesh size of $8d_0$. The dimensionless undercooling is set to be $\Delta T/(|m|(1-k)C_0) = 0.7$. In this case, the simulated steady-state tip equilibrium composition $C_l^*/C_0 = 1.533$. The dimensionless supersaturation can be calculated by Eq. (16) as $\Omega = 0.42$. The steady-state velocity and radius of the upstream tip are determined as described in Section 3.3. The tip radius is measured based on a parabolic fitting to the simulated dendrite shape as described in Ref. [25]. The simulated growth Péclet number and flow Péclet number can then be calculated with $P_c = VR/(2D_l)$ and $P_f = U_{in}R/(2D_l)$, respectively. A comparison between the numerical simulations and the Oseen–Ivantsov solutions for the growth Péclet number as a function of the flow Péclet number is presented in Fig. 12. It should be noted that the simulated growth Péclet numbers, increasing with the flow Péclet numbers, appear to be very close to those predicted by the Oseen–Ivantsov solution.

Using a linear solvability analysis, Bouissou and Pelce [39] studied the effect of flow on the selection parameter and deduced that the ratio of the selection parameters without flow and with flow, $(\sigma^*)_0/\sigma^*$, is a function of a dimensionless flow parameter, $\chi = a(\mathrm{Re})Ud_0/(\beta^{3/4}RV)$, where $\beta = 15\varepsilon$ and $a(\mathrm{Re}) = \sqrt{2\mathrm{Re}/\pi}\exp(-\mathrm{Re}/2)/erfc(\sqrt{\mathrm{Re}/2})$. When χ is large enough, the relationship has the form: $(\sigma^*)_0/\sigma^* \cong 1 + b\chi^{11/14}$, where b is a constant. However, when the flow is weak and χ is much smaller than unity, the ratio of $(\sigma^*)_0/\sigma^*$ is independent of the flow parameter, i.e. $(\sigma^*)_0/\sigma^* \cong 1$. We performed the simulations in the small χ regime $(0 < \chi < 0.2)$ with two undercoolings of $\Delta T/(|m|(1-k)C_0) = 0.6$ and 0.7, corresponding to the dimensionless supersaturation $\Omega = 0.37$ and 0.42, respectively. Other simulation conditions are identical to those of Fig. 12. As shown in Fig. 13, the simulated ratios of $(\sigma^*)_0/(\sigma^*)$ with various flow parameters χ are all close to unity for two supersaturations, which coincides with the prediction of the linear solvability theory. Tong et al. [2] carried out simulations using a PF-NS model for convective dendritic growth of a pure substance in the same small χ regime $(0 < \chi < 0.2)$, and also found that the ratio of $(\sigma^*)_0/(\sigma^*)$ based on a parabolic fitted radius is indeed nearly independent of the flow parameter χ for various surface energy anisotropy coefficients and dimensionless undercoolings.

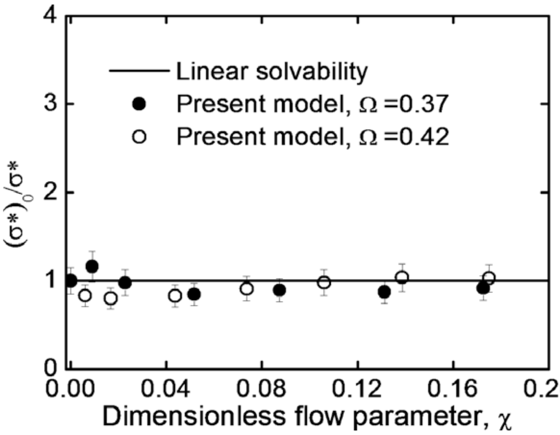

Fig. 13. Comparison between the numerical simulations and the linear solvability theory prediction for the ratio of the selection parameters without and with flow as a function of the dimensionless flow parameter χ.

3.4.3. Comparison with the ZS-NS model

To further examine the potential of the present model, the ZS-NS model, in which the fluid flow and solute transport are calculated using a NS solver based on the SIMPLE (Semi-Implicit Method for Pressure-Linked Equations) algorithm, is adopted to simulate single convection-free dendritic growth under identical conditions to those used in Fig. 9. The time histories of the evolution of the solid fraction simulated from the two models are compared in Fig. 14. It can be seen that the agreement between the predictions of the two numerical models is good, although there is a slight deviation between the profiles when the solid phase fraction increases to higher values. This deviation is considered to be caused by the

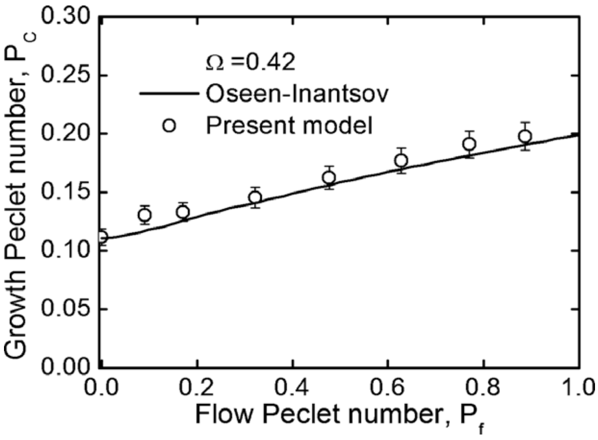

Fig. 12. Comparison between the numerical simulations and the 2D Oseen–Ivantsov solution for the growth Péclet number as a function of the flow Péclet number (Ω: the dimensionless supersaturation).

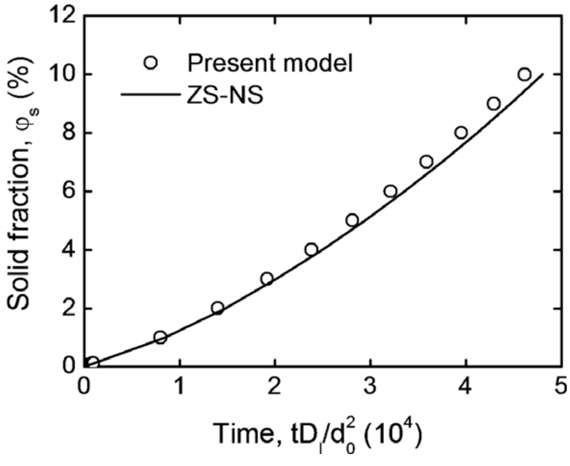

Fig. 14. Evolution of solid fraction with time for an Al–3 wt.% Cu alloy solidified with a constant undercooling $\Delta T/(|m|(1-k)C_0) = 0.7$ and an inlet flow velocity $U_{in}d_0/\nu = 0.0015$: comparison between the present model and the ZS-NS (Zhu and Stefanescu – Navier – Stokes) model.

different schemes used in the two models for treating the nonslip boundary condition at the SL interface. Nevertheless, the result of Fig. 14 indicates that the LB equation for the fluid flow calculation converges to the NS equation. Furthermore, it is interesting to note that the present model is computationally quite efficient. It requires about 0.5 μs per grid point and per time step on a PC Core 2 Duo, 2.67 GHz CPU. The calculation time of the present model for the results shown in Fig. 9 is about 18 min, which is about nine times faster than that required for the ZS-NS model (about 160 min).

3.5. Equiaxed multidendritic growth

The present model is applied to simulate the formation of multiequiaxed dendrites during alloy solidification for the two cases of pure diffusion and diffusion together with melt convection. The calculation domain is divided into 400 × 400 mesh points with a mesh size of 1 μm. At the start of the simulation, several seeds with randomly assigned preferred growth orientations are placed on the domain. The temperature in the domain is assumed to be uniform and cooled down from liquidus temperature at a cooling rate of 10 K s^{-1}. The simulations are stopped when the domain temperature reaches the eutectic temperature. Fig. 15 presents the simulated evolution of multiequiaxed dendrites for an Al–4.5 wt.% Cu alloy. The figures in the upper row show dendrites formed by pure diffusion and those in the bottom row show dendrites formed under convective boundary conditions of a forced flow with an inlet flow velocity of $U_{in} = 0.001$ m s^{-1}. It can be noted that during pure diffusion-controlled solidification the main arms of the dendrites develop along their crystallographic orientations, followed by the growth and coarsening of the primary trunks together with the branching of the secondary arms. However, the growth of the primary trunks and side branches might be affected by the nearby dendrites. On the other hand, when dendrites grow under the influence of melt convection, solute atoms are at the early growth stage transported from the upstream side to the downstream side of each dendrite by the flowing melt, resulting in asymmetric dendrite morphologies. As solidification proceeds, primary arms grow and coarsen with the evolution of side branches. The primary and secondary arms are all distinctly deflected to the upstream direction. As the dendrites grow close to each other, the fluid flow almost vanishes in the interdendritic region. Thus, at the later stage the growth of dendrites is not affected much by the flow. Moreover, it can be noted that the solute content in the liquid phase increases as solidification proceeds. Consequently,

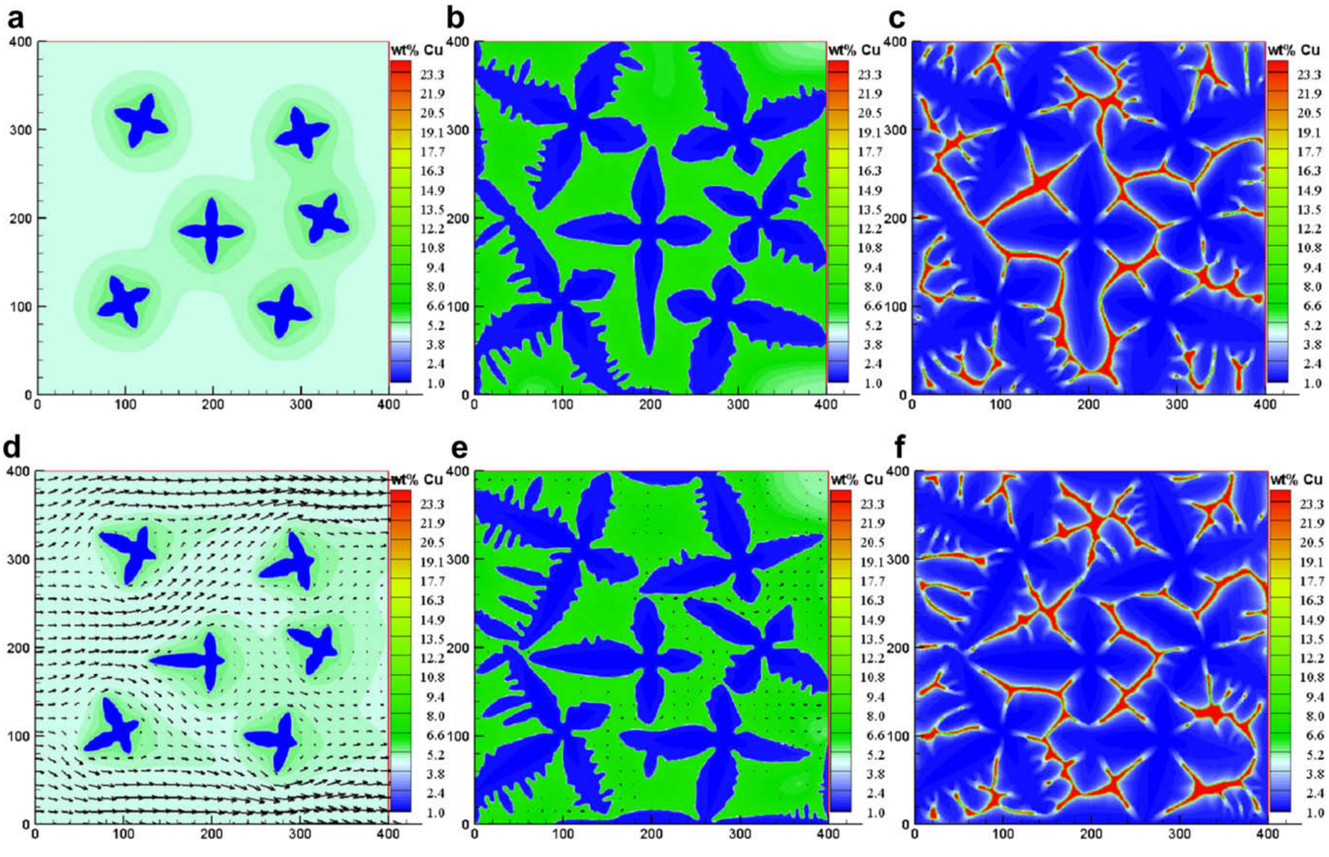

Fig. 15. Evolution of multiequiaxed dendrites for an Al–4.5 wt.% Cu alloy solidified with a cooling rate of 10 K s^{-1}: (a,d) $\varphi_s = 0.06$, (b,e) $\varphi_s = 0.45$, (c,f) $\varphi_s = 0.93$ (φ_s: solid volume fraction). Here (a–c) show dendrites formed by pure diffusion and d–f show dendrites formed under convective boundary conditions of a forced flow with an inlet flow velocity of $U_{in} = 0.001$ m s^{-1}.

the outside shell of the dendrites, where the final solidification of the solute-enriched liquid occurs, reveals a higher solute concentration as shown in Fig. 15c and f.

As presented in the previous section, the present model is computationally more efficient than the ZS-NS model for the simulation of single-convective dendritic growth. Again, for comparison the ZS-NS model is also applied to the present case of multidendritic growth under the same conditions as used in Fig. 15. However, because of the divergence in the flow calculation, the ZS-NS simulation cannot be performed when the solid fraction is above about 0.25. Accordingly, it is apparent that the present LBM-based model has the significant advantages of a good numerical stability and computational efficiency for the simulation of dendritic growth in the presence of melt convection.

4. Conclusions

A LBM-based model is presented for modeling solutal dendritic growth with melt convection. In the model, the momentum and species transfers are numerically solved by the kinetic-based LBM, rather than via a continuum-based NS solver. The LB solute distribution function is incorporated via a flow velocity vector and a source term that accounts for the solute partition at the SL interface, which allows valid computations of solute transport controlled by both convection and diffusion during phase transition. Based on the LBM-calculated solutal field, the evolution of the SL interface can be determined according to a local solute equilibrium approach. The mesh dependency of the present model for the simulation of convective dendritic growth is evaluated. The calculated steady-state growth velocity of the upstream tip is found to converge to a finite value when the mesh is refined. Extensive model validation has been carried out through comparison of the simulation results with available analytical models. First, the LB simulations for 1D solute diffusion and 2D Stokes flow past regular arrays of infinite cylinders coincide well with the analytical solutions. Second, the simulated steady-state tip features, including tip velocity, tip radius, equilibrium composition, and Péclet number, as functions of undercoolings for purely diffusive dendritic growth of an Al–3 wt.% Cu alloy, are compared with the analytical LGK predictions. The agreement appears to be quite reasonable. Third, for convective dendritic growth in a forced flow, the simulated growth Péclet number of the upstream tip as function of the flow Péclet number is very close to the analytical Oseen–Ivantsov solution. In addition, the ratio of the selection parameters without flow and with flow is in good agreement with the prediction of the linearized solvability theory. The proposed model is applied to simulate both single- and multiequiaxed dendritic growth of Al–Cu alloys in a forced flow. The simulation results show that the dendritic growth behavior is significantly affected by melt convection. The dendritic growth is promoted and hindered in the upstream and downstream regions, respectively. However, the growth of the perpendicular tip is not greatly affected by fluid flow. The evolution of multiequiaxed dendrites with various orientations is also reproduced. The simulation results illustrate the interaction of fluid flow, solute transport and phase transition during alloy solidification. It is found that at the early stage of solidification, primary arms and side branches are distinctly deflected towards the incoming fluid flow, whereas the flow effect on dendritic growth gradually weakens as the dendrites grow close to each other. The comparison with the ZS-NS model indicates that the present model is more numerically stable and computationally efficient, as well as simpler to implement for the simulation of phase transition problems coupled with melt convection.

Acknowledgments

The authors thank Professor Doru Stefanescu at the Ohio State University for the helpful discussion. This work was supported by the National Natural Science Foundation of China under Grant (Grant No. 50671025) and the Specialized Research Fund for the Doctoral Program of Higher Education of China (Grant No. 20070286021).

References

[1] Beckermann C, Diepers H-J, Steinbach I, Karma A, Tong X. J Comput Phys 1999;154:468.
[2] Tong X, Beckermann C, Karma A, Li Q. Phys Rev E 2001;63:061601.
[3] Lan CW, Shih CJ. Phys Rev E 2004;69:031601.
[4] Lan CW, Shih CJ. J Cryst Growth 2004;264:472.
[5] Al-Rawahi N, Tryggvason G. J Comput Phys 2004;194:677.
[6] Tan L, Zabaras N. J Comput Phys 2006;211(1):36.
[7] Tan L, Zabaras N. J Comput Phys 2007;221:9.
[8] Shin YH, Hong CP. ISIJ Int 2002;42:359.
[9] Zhu MF, Lee SY, Hong CP. Phys Rev E 2004;69:061610.
[10] Zhu MF, Dai T, Lee SY, Hong CP. Sci China E 2005;48(3):241.
[11] Zhu MF, Dai T, Lee SY, Hong CP. Comput Math 2008;55:1620.
[12] Li DM, Li R, Zhang PW. Appl Math Modell 2007;31:971.
[13] Raabe D. Modell Simul Mater Sci Eng 2004;12:R13.
[14] Succi S. Eur Phys J B 2008;64:471.
[15] Shi Y, Zhao TS, Guo ZL. Phys Rev E 2006;73:026704.
[16] Carolin K, Thies M, Thomas H, Nils T, Ulrich R. J Stat Phys 2005;121(1/2):179.
[17] Varnik F, Raabe D. Modell Simul Mater Sci Eng 2006;14:857.
[18] Varnik F, Truman P, Wu B, Uhlmann P, Raabe D, Stamm M. Phys Fluids 2008;20:072104.
[19] Miller W, Succi S, Manutti D. Phys Rev Lett 2001;86(16):3578.
[20] Miller W, Succi S. J Stat Phys 2002;107:173.
[21] Miller W, Rasin I, Pimentel F. J Cryst Growth 2004;266:283.
[22] Medvedev D, Kassner K. Phys Rev E 2005;72:056703.
[23] Medvedev D, Fischaleck T, Kassner K. J Cryst Growth 2007;303:69.
[24] Chatterjee D, Chakraborty S. Phys Lett A 2006;351:359.
[25] Zhu MF, Stefanescu DM. Acta Mater 2007;55:1741.
[26] Chen S, Chen H, Martinez D, Matthaeus WH. Phys Rev Lett 1991;67(27):3776.
[27] Qian YH, D'Humibres D, Lallemand P. Europhys Lett 1992;17(6):479.
[28] Deng B, Shi BC, Wang GC. Chin Phys Lett 2005;22(2):267.
[29] Chapman S, Cowling TG. The mathematical theory of non-uniform gases. 3rd ed. Cambridge: Cambridge University Press; 1970.
[30] Guo ZL, Zheng CG, Shi BC. Chin Phys 2002;11(4):366.
[31] Maier RS, Bernard RS, Grunau DW. Phys Fluids 1996;8(7):1788.

[32] Belteran-Sanchez L, Stefanescu DM. Metall Mater Trans A 2004;35:2471.
[33] Sangani AS, Acrivos A. Int J Multiphase Flow 1982;8(4):343.
[34] Lipton J, Glicksman ME, Kurz W. Mater Sci Eng 1984;65:57.
[35] Lipton J, Glicksman ME, Kurz W. Metall Trans A 1987;18A:341.
[36] Trivedi R, Kurz W. Int Mater R 1994;39(2):49.
[37] Stefanescu DM. Science and engineering of casting solidification. New York: Kluwer Academic/Plenum Publishers; 2002.
[38] Barbieri A, Langer S. Phys Rev A 1989;39:5314.
[39] Bouissou Ph, Pelce P. Phys Rev A 1989;40:6673.